ARTICLES
PUBLISHED ONLINE: 19 JUNE 2017 | DOI: 10.1038/NNANO.2017.54
nature nanotechnology

Neutrophil-mediated anticancer drug delivery for suppression of postoperative malignant glioma recurrence

Jingwei Xue, Zekai Zhao, Lei Zhang, Lingjing Xue, Shiyang Shen, Yajing Wen, Zhuoyuan Wei, Lu Wang, Lingyi Kong, Hongbin Sun, Qineng Ping, Ran Mo* and Can Zhang*

Cell-mediated drug-delivery systems have received considerable attention for their enhanced therapeutic specificity and efficacy in cancer treatment. Neutrophils (NEs), the most abundant type of immune cells, are known to penetrate inflamed brain tumours. Here we show that NEs carrying liposomes that contain paclitaxel (PTX) can penetrate the brain and suppress the recurrence of glioma in mice whose tumour has been resected surgically. Inflammatory factors released after tumour resection guide the movement of the NEs into the inflamed brain. The highly concentrated inflammatory signals in the brain trigger the release of liposomal PTX from the NEs, which allows delivery of PTX into the remaining invading tumour cells. We show that this NE-mediated delivery of drugs efficiently slows the recurrent growth of tumours, with significantly improved survival rates, but does not completely inhibit the regrowth of tumours.

Glioblastoma, the most-invasive brain tumour, is characterized by the highest mortality rate, short lifetime and poor prognosis with a high tendency of recurrence[1–3]. Surgery is applied to excise the tumour bulk[4], but the infiltrating tumour cells inside the normal brain parenchyma cannot be completely removed because of damage to the healthy brain[5]. These residual tumour cells are protected by the blood–brain barrier (BBB)[6] or blood–brain-tumour barrier (BBTB), which impedes the delivery of chemotherapeutics[7], and so tumour recurrence occurs. Although nanoparticle-based drug-delivery systems (DDSs) show capacity for enhanced tumour targetability[8–11], these DDSs cannot achieve full therapeutic potential for postoperative glioma treatment because the predominant distribution of particles is in the perivascular space of the recrudescent tumour and because of a low intratumoural drug concentration[12,13].

Vectorization of therapeutic agents using endogenous cells has been proposed as a strong potential strategy for brain-targeted drug delivery[14–16]. Neutrophils (NEs) have a native ability to traverse BBB/BBTB[17,18] and penetrate the glioma site[19,20]. Tumour-associated NEs (TANs) have been found to be distributed in the glioma region[21], which also have a positive effect on the continuous recruitment of the circulating NEs[22]. More importantly, surgical tumour removal leads to the occurrence of local brain inflammation with the release of the inflammatory factors, such as interleukin-8 (IL-8)[23,24] and tumour necrosis factor α (TNF-α)[25,26], which activate NEs for migrating to the inflamed brain[27]. This amplification of inflammatory signals supports an enhanced brain-tumour targeting.

Herein we report the application of NEs that carry paclitaxel (PTX)-loaded liposomes to suppress postoperative glioma recurrence (Fig. 1). PTX, a model small-molecule drug for glioma treatment[28,29], is encapsulated into cationic liposomes (PTX-CL), followed by the NE internalization to obtain NE-based delivery vehicles (PTX-CL/NEs) (Fig. 1a). After surgical tumour resection, an inflammation reaction occurs in the brain, accompanied by the release of inflammatory factors into the blood (Fig. 1b). The subsequently intravenously administrated PTX-CL/NEs are primed by the chemoattractants and migrate along the chemotactic gradient towards the infiltrating tumour cells in the inflamed brain via a conformational change[30] in which PTX-CL/NEs are activated excessively by concentrated activating signals and release neutrophil extracellular traps (NETs)[31,32], which results in a concomitant release of PTX-CL. PTX-CL can deliver PTX efficiently into the tumour cells and induce cytotoxicity to inhibit tumour recurrence (Fig. 1c).

Preparation and characterization of PTX-CL/NEs

PTX-CL that contain $HG2C_{18}$ (Supplementary Fig. 1) were prepared with an average particle size of 100 nm (Fig. 2a) and a positive surface charge (Supplementary Fig. 2a,b). A sustained release of PTX was achieved by liposomal encapsulation (Supplementary Fig. 2c). The mature NEs were isolated from the mouse bone marrow and purified by density-gradient centrifugation[33] with a yield of about 6.5×10^6 cells/mouse. The viability was determined to be 98.9%, and the purity was quantified to be higher than 90% (Fig. 2b).

PTX-CL/NEs were obtained by incubating the purified NEs with PTX-CL, and collected by centrifugation. Compared with Taxol, which produces a greater cytotoxicity at high concentrations, PTX-CL had negligible toxicities towards NEs at all the studied concentrations with 12 hours of incubation (Supplementary Fig. 3), which laid a foundation for NEs to be loaded with PTX-CL. PTX-CL can be taken up efficiently by NEs (Supplementary Fig. 4). The resulting PTX-CL/NEs had a loading capacity of 18 μg PTX/10^6 cells. No significant morphological change of NEs was observed after loading with PTX-CL (Fig. 2c).

The physiological functions of PTX-CL/NEs in response to inflammatory cues were evaluated, including specific protein expression, chemotaxis and superoxide-generating ability. CD11b, an NE-specific surface protein, regulates the adhesion and migration of NEs[34,35], which is upregulated on the occurrence of inflammation. As expected, the CD11b expression level of PTX-CL/NEs dramatically rose after treatment with formylmethionylleucylphenylalanine (fMLP),

State Key Laboratory of Natural Medicines, Jiangsu Key Laboratory of Drug Discovery for Metabolic Diseases, Center of Advanced Pharmaceuticals and Biomaterials, China Pharmaceutical University, Nanjing 210009, China. *e-mail: rmo@cpu.edu.cn; zhangcan@cpu.edu.cn

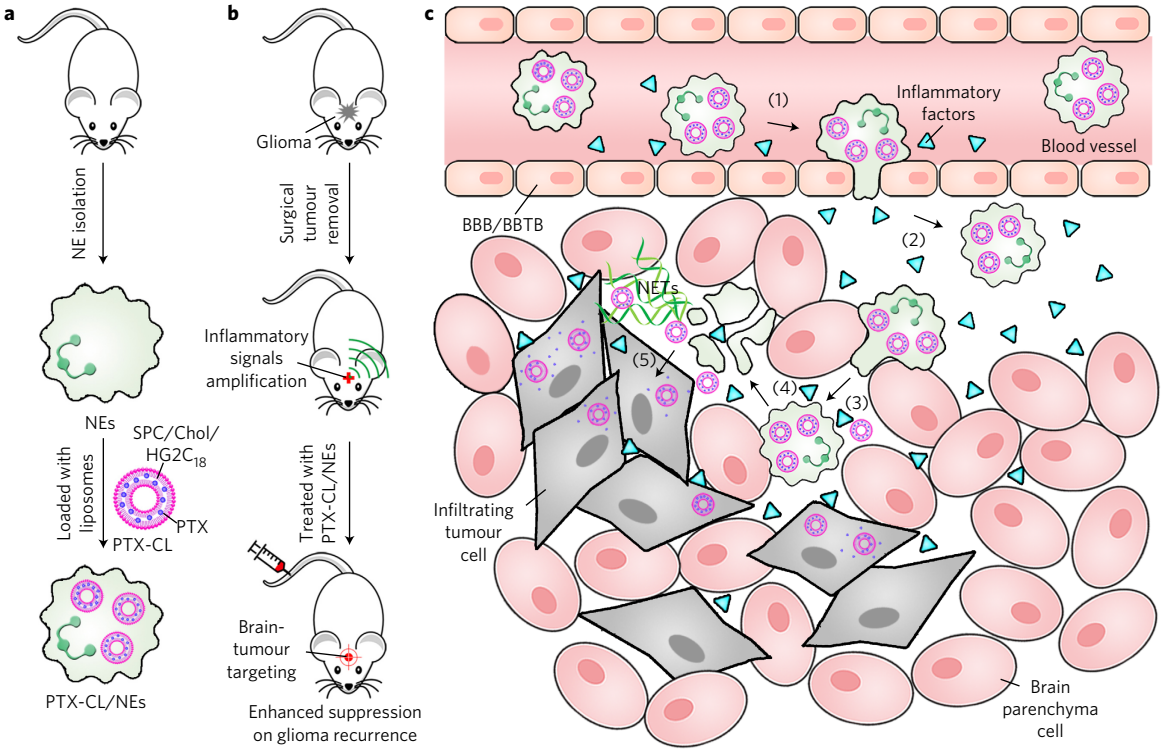

Figure 1 | Schematic design of NE-mediated anticancer drug delivery for the suppression of postoperative glioma recurrence. a, Schematic illustration of the preparation of PTX-CL/NEs. SPC, soy phosphatidylcholine; Chol, cholesterol; $HG2C_{18}$, 1,5-dioctadecyl-*N*-histidyl-L-glutamate. **b**, Schematic that shows how PTX-CL/NEs suppress postoperative glioma recurrence in mice. Surgical resection of a tumour amplifies inflammatory signals in the brain, which allows PTX-CL/NEs to target brain tumours, release PTX and suppress glioma recurrence. **c**, Schematic that shows how PTX-CL/NEs target glioma after intravenous injection into mice whose brain tumour has been resected surgically: (1) inflammatory factors guide the movement of PTX-CL/NEs along the chemotactic gradient; (2) PTX-CL/NEs transmigrate to the inflamed brain across BBB/BBTB; (3) PTX-CL/NEs penetrate the infiltrating tumour cells; (4) PTX-CL/NEs are excessively activated by the concentrated cytokines and release the NETs, which results in a concomitant release of PTX-CL; and (5) PTX-CL delivers PTX into the infiltrating tumour cells to produce an antitumour effect. NETs that primarily consist of DNA from NEs are fibrous extracellular matrices, which were released by NEs on excessive activation by inflammatory cytokines.

an NE chemotactic peptide[36,37] (Fig. 2d). No substantial difference was determined in the increased CD11b level between PTX-CL/NEs and the blank NEs. Furthermore, a transwell migration assay[38] demonstrated that PTX-CL/NEs presented fMLP-activated chemotaxis comparable to that of both NEs and CL/NEs (NEs that contain the blank CL), whereas Taxol/NEs (NEs that contain Taxol) almost fully lost the chemotactic function (Fig. 2e and Supplementary Fig. 5). This migration capacity of PTX-CL/NEs was fMLP-concentration dependent. Additionally, treatment with fMLP resulted in a significantly increased level of superoxide anion in PTX-CL/NEs, which had an equivalent effect on NEs (Fig. 2f). Taken together, PTX-CL/NEs maintain the physiological activities of NEs, which can actively respond to the inflammatory stimuli and directionally migrate to the inflammation site.

We next explored the stability and release of PTX-CL in/from NEs under different conditions: in a normal physiological environment, during the chemotactic process and at the site of inflammation. fMLP and phorbol myristate acetate (PMA)[31] were applied to simulate the inflammatory factors in the blood circulation and at the inflammatory site, respectively. At physiological conditions, the quantity of PTX was maintained in NEs for eight hours, and very little PTX was released from the NEs (Fig. 2g). Similarly, PTX-CL/NEs were stable, with negligible leakage of PTX after treatment with fMLP (Fig. 2h). In contrast, PTX-CL/NEs showed a burst release of PTX after four hours of incubation with PMA (Fig. 2i). The apoptosis of NEs induced by sulfasalazine[39] caused a slight release of PTX (Supplementary Fig. 6). Compared with the untreated or fMLP-treated Cou6-CL/NEs (NEs that carry coumarin-6-labelled CL), PMA-treated Cou6-CL/NEs presented a nearly completely release of Cou6 and an evident formation of NETs[40], as shown by propidium iodide (PI) staining (Supplementary Fig. 7). Quantitative analysis showed that about 88% of the PTX released from NEs was encapsulated in the liposomes. An intact structure of the released PTX-CL was observed (Supplementary Fig. 8). These data indicate that PTX-CL/NEs can preserve stability during the recruitment process, but rapidly release PTX-CL, accompanied by the release of NETs because of excessive activation by the concentrated activating signals at the inflammatory site[31,40].

Inflammation-directed sequential delivery to tumour

The well-established murine-brain microvascular endothelial (bEnd.3) cell monolayer (Supplementary Fig. 9) as an *in vitro* BBB model[41,42] was employed to estimate the BBB penetration capability of PTX-CL/NEs (Fig. 3a). At physiological conditions, all the tested PTX formulations showed extremely low permeability through the monolayer (Fig. 3b). The quantity of PTX delivered by PTX-CL/NEs in the lower chamber was only 1%. Nevertheless, the PTX quantity of PTX-CL/NEs at the basolateral side dramatically increased to 38% under inflamed conditions in the presence of fMLP (Fig. 3c), and nearly 35% of NEs across the monolayer was found (Supplementary Fig. 10a). A corresponding decrease in the amount of PTX was found at the apical side, whereas no significant change of the intracellular PTX quantity was determined. However, neither Taxol nor PTX-CL showed any improvement on the PTX permeation under inflammatory conditions. Treatment with

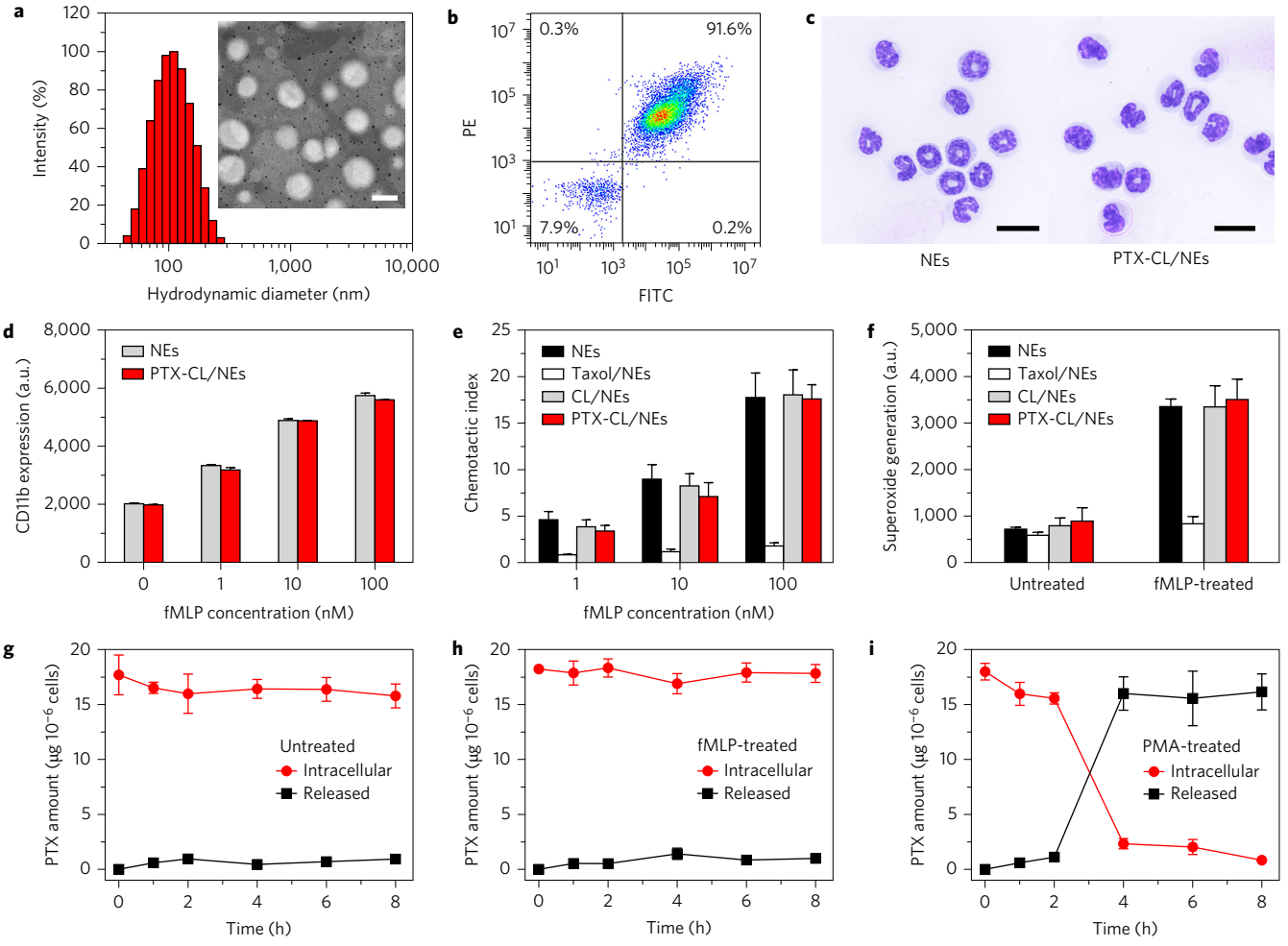

Figure 2 | Preparation and characterization of PTX-CL/NEs. a, Histogram of particle-size distribution of PTX-CL obtained by dynamic light scattering measurements. Inset: the transmission electronic microscope image of PTX-CL. Scale bar, 200 nm. **b**, Flow cytometric analysis of the purity of NEs doubly stained with FITC-conjugated Gr-1 and PE-conjugated MAIR-IV antibodies. The lower-left, lower-right, upper-left and upper-right quadrants in the panel represent the populations of $FITC^-/PE^-$, $FITC^+/PE^-$, $FITC^-/PE^+$ and $FITC^+/PE^+$ cells, respectively. The average population of the cells is shown in the corner of each quadrant. **c**, Morphological images of NEs (left) and PTX-CL/NEs (right) stained with Wright-Giemsa. The obtained NEs show a typical lobulated shape of nuclei with many light-pink granules in the cytosol. Scale bars, 10 μm. **d**, Change in the expression level of CD11b on the cell membrane of PTX-CL/NEs after treatment with different concentrations of fMLP for 0.5 h ($n = 2$ independent experiments). CD11b was stained with PE-conjugated CD11b antibody. **e**, Chemotaxis of PTX-CL/NEs after treatment with different concentrations of fMLP for 0.5 h ($n = 3$ independent experiments). The chemotactic index was obtained using a transwell migration assay. **f**, Superoxide generation of PTX-CL/NEs after treatment with fMLP (1 μM) for 0.5 h ($n = 3$ independent experiments). PTX-CL/NEs were stained with dihydroethidium. **g**–**i**, Determination of the quantity of PTX released from and retained in PTX-CL/NEs in the absence of fMLP (**g**) and in the presence of fMLP (10 nM) (**h**) and of PMA (100 nM) (**i**) over time ($n = 3$ independent experiments). In **d**–**i**, the data are shown as mean ± s.d.

PTX-CL/NEs produced a rapid reduction in the transendothelial electrical resistance (TEER) value of the bEnd.3 cell monolayers compared with that by Taxol or PTX-CL (Supplementary Fig. 10b), which is partly a result of the opening of tight junctions between neighbouring endothelial cells. The results suggest that the inflammation-primed PTX-CL/NEs can migrate efficiently across BBB into the inflamed brain for an enhanced permeability and brain targeting.

The tumour-penetration ability of the NE-based formulation was evaluated using a three-dimensional (3D) multicellular tumour spheroid model[43]. The upregulation of cytokines, including TNF-α and CXCL1/KC (refs 44,45), a mouse homologue of IL-8 with an NE chemoattractant activity equivalent to human IL-8, was first confirmed in the established murine glioblastoma (G422) tumour spheroid (Supplementary Fig. 11). A concentration gradient was present between intratumoural and extratumoural sites. The cell membranes of Cou6-CL/NEs were stained with 1,1′-dioctadecyl-3,3,3′,3′-tetramethylindotricarbocyanine iodide (DiR) to achieve double-stained Cou6-CL/DiR-NEs, in which the Cou6 and DiR signals were clearly observed within the cells and on the cell membrane, respectively (Supplementary Fig. 12). After incubation with Cou6-CL/DiR-NEs, both Cou6 and DiR signals were monitored simultaneously in real time from the surface to the middle of the tumour spheroid at a depth of 120 μm (Supplementary Fig. 13). The Cou6 signal was visualized to penetrate gradually into the middle of the tumour, and uniformly distribute in most areas of the tumour after eight hours of incubation, which indicates that Cou6-CL/DiR-NEs are capable of permeating nearly 80% of a tumour spheroid with an average diameter of 300 μm. A high degree of co-localization between the Cou6 and DiR signals was found, which suggests that the liposomes were encapsulated stably in the NEs during the penetration process. Comparatively, at such a depth, the Cou6 signal was observed only on the periphery of the tumour spheroid treated with either the Cou6 solution or Cou6-CL (Fig. 3d).

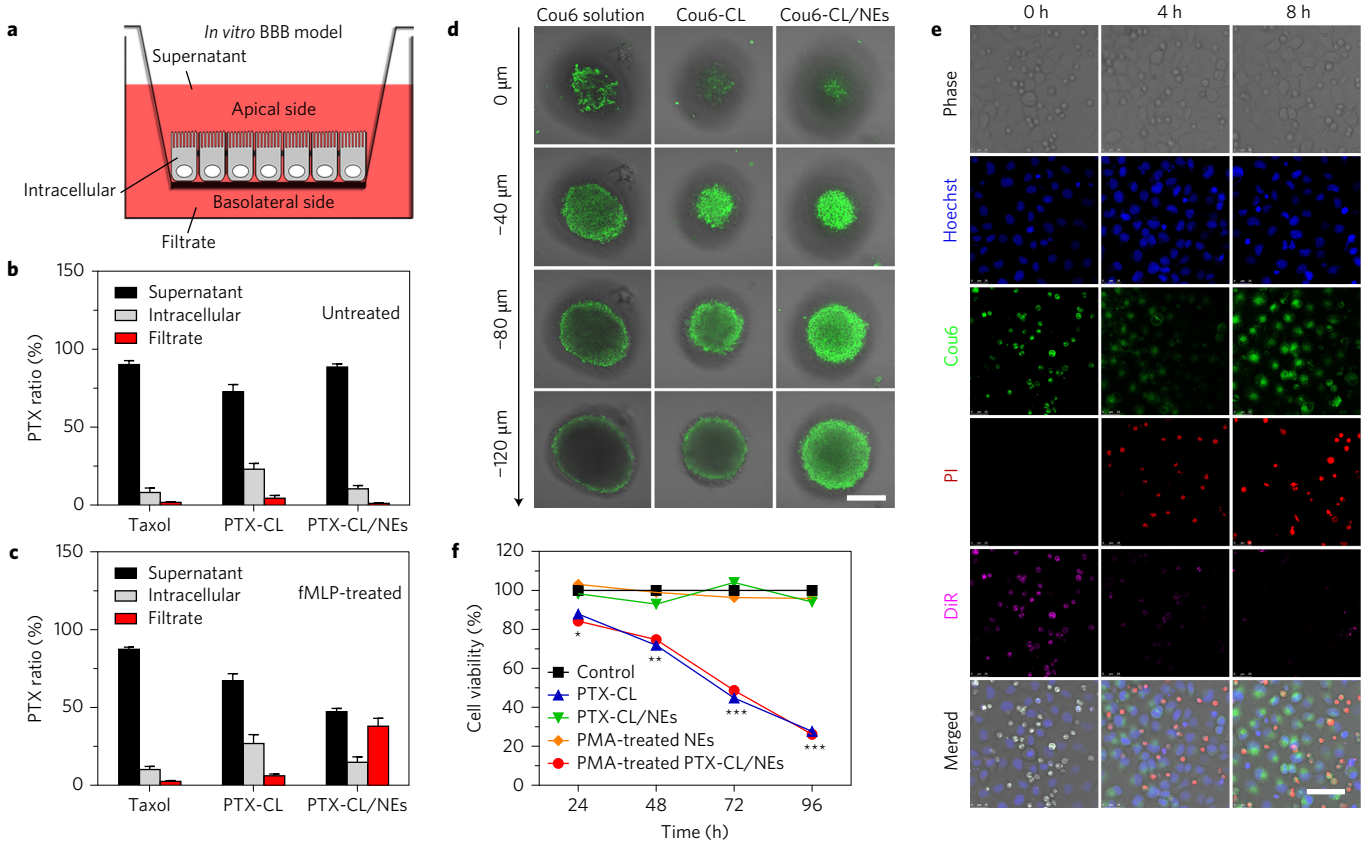

Figure 3 | Inflammation-directed sequential delivery. a, Schematic illustration of the *in vitro* BBB model using a transwell system to evaluate the penetration capability of PTX-CL/NEs across the endothelial monolayer. Quantities of PTX were determined in the supernatant (apical side), endothelial layer (intracellular) and filtrate (basolateral side). **b**,**c**, Quantification of the PTX distribution in the transwell chamber after incubation with different PTX formulations in the absence of fMLP (**b**) and in the presence of fMLP (10 nM) (**c**) for 3 h. Data are shown as mean ± s.d. ($n = 3$ independent experiments). **d**, Penetration of Cou6 into the 3D G422 tumour spheroids after incubation with different Cou6 formulations for 8 h. CLSM images were obtained from the surface to the middle of the tumour spheroids in a *Z*-stack thickness of 40 μm. Scale bar, 150 μm. **e**, CLSM images of G422 cells after incubation with Cou6-CL/DiR-NEs (1×10^5 cells, equivalent to 16.5 ng ml^{-1} Cou6) treated with PMA (100 nM) over time. The nuclei of G422 cells were stained with Hoechst 33342, and the released DNA segments were stained with PI. The merged image is the overlay of five individual images. Scale bar, 50 μm. **f**, Cytotoxicity of PMA-treated PTX-CL/NEs (0.83×10^6 cells ml^{-1}, equivalent to 15 μg ml^{-1} PTX) against G422 cells for different times. Data are shown as mean ± s.d. ($n = 3$ independent experiments). $^*P < 0.05$, $^{**}P < 0.01$, $^{***}P < 0.001$, PMA-treated PTX-CL/NEs compared with untreated PTX-CL/NEs (two-tailed Student's *t*-test).

We further assessed the inflammation-driven intercellular trafficking of drug from NEs to the targeted cancer cells (Fig. 3e). When Cou6-CL/DiR-NEs was added initially into the G422 cell monolayer, both Cou6 and DiR signals were apparent, whereas no PI signal was detected. After four hours of incubation with PMA, Cou6-CL/DiR-NEs released Cou6-CL, accompanied by the formation of NETs and the attenuation of the DiR signal, which indicates the disruption of the NE plasma membrane. As time extended to eight hours, the released Cou6-CL was endocytosed by G422 cells. Contrarily, the Cou6 signal was visualized only within the NEs rather than the G422 cells in the absence of PMA over time (Supplementary Fig. 14). Accordingly, NEs can release their encapsulated liposomes, which carry drugs and permeate into the glioma cells, on excessive activation at the inflammation site.

The antiproliferation of PMA-treated PTX-CL/NEs against G422 cells was investigated (Fig. 3f and Supplementary Fig. 15). PTX-CL/NEs pre-treated with PMA presented a comparable cytotoxicity to that of PTX-CL, whereas the untreated PTX-CL/NEs without the release of PTX-CL did not have any antiproliferative activity at all the studied concentrations. In addition, PMA-treated NEs presented insignificant cytotoxicity towards G422 cells. These findings suggest that PTX-CL, which were released from NEs in response to the inflammatory stimuli, can effectively deliver PTX into the glioma cells to produce an antitumour effect.

Postoperative upregulation of pro-inflammatory cytokines

A glioma surgical resection model[46] was constructed (Fig. 4a). First, G422 cells were intracranially injected into the mice to generate a mouse *in situ* glioma model, followed by a histological examination (Supplementary Fig. 16). At 16 days post-implantation, the tumours presented a prominently greater infiltration pattern, which showed apparently wider projections of invading tumour cells together with many more islands of tumour cells, both around the primary tumour mass and inside the surrounding normal brain parenchyma (Fig. 4b). TANs could be found in the tumour (Supplementary Fig. 17). Meanwhile, we used stable luciferase-transfected G422 (Luc-G422) cells to monitor constantly the initial tumour growth. An increase in luminescence intensity was observed in the brain during the 16 days after the intracranial implantation of Luc-G422 cells (Supplementary Fig. 18a,b).

A time point of 16 days after implantation of the G422 cells was selected as the appropriate time for surgery to construct the glioma resection model (Fig. 4c). The glioma-bearing mice were able to tolerate the operative procedure with a low mortality rate (<5%) and the absence of neurological impairment after surgery. We

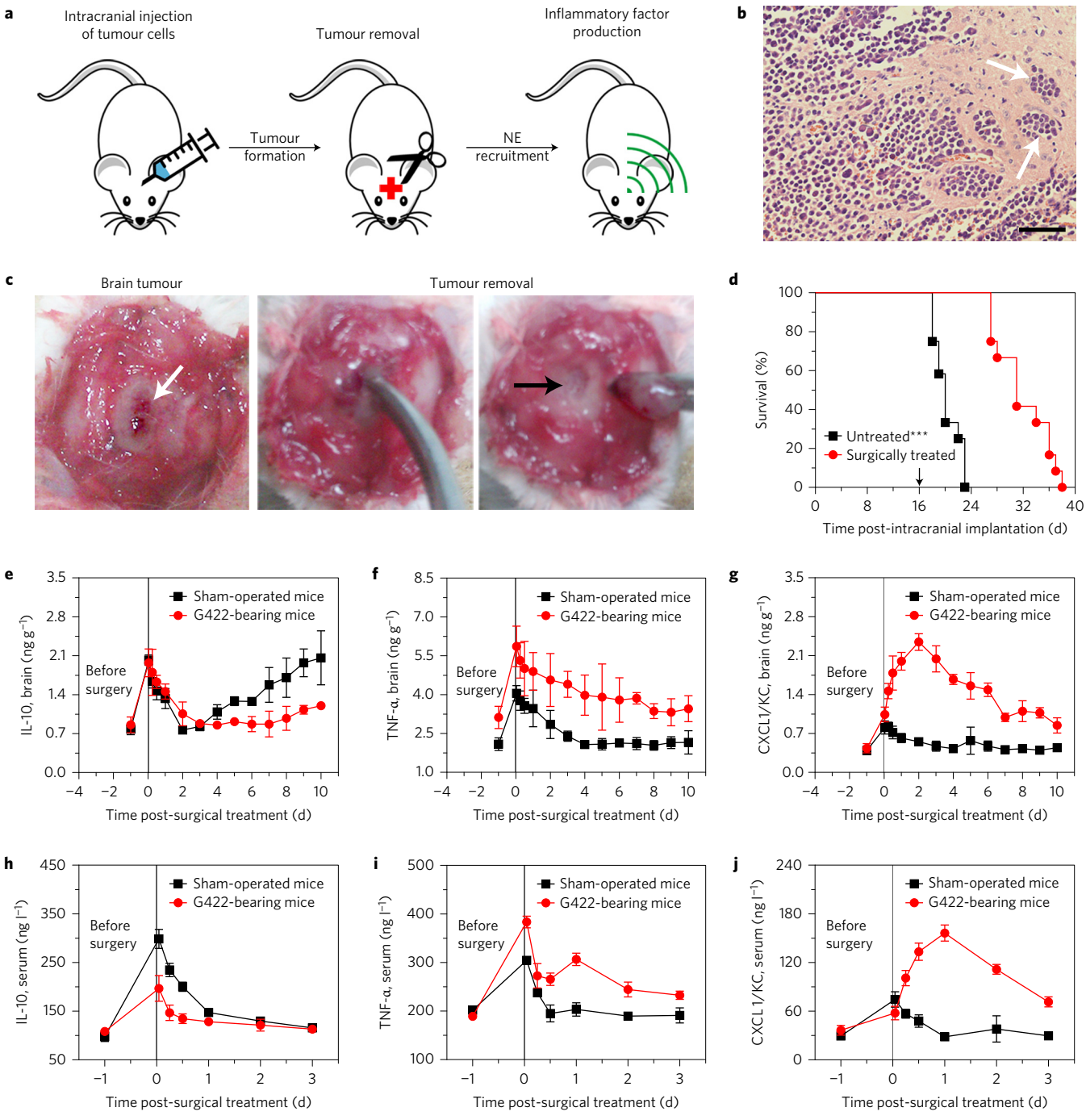

Figure 4 | Pro-inflammatory cytokines are upregulated in the glioma surgical resection model. a, Schematic illustration of the construction of the G422 glioma surgical resection model. **b**, Histological observation of the brain collected from the mice after G422 tumour implantation for 16 days. The brain section was stained with H&E. White arrows indicate islands of tumour cells around the primary tumour mass and inside the surrounding normal brain parenchyma. Scale bar, 100 μm. **c**, Process of surgical tumour removal from the brain of the G422-bearing mice. Left, image of the formed G422 tumour (white arrow) in the brain of the mice at 16 d post-implantation; middle, microsurgical removal of the tumour from the brain; right, surgical cavity (black arrow) that remains after the tumour removal and the surrounding white region of the normal brain. **d**, Survival curves of the G422-bearing mice without and with surgical treatment ($n = 12$ mice per group). Arrow indicates the time of the surgery. ***$P < 0.001$, untreated compared with surgically treated (log-rank (Mantel–Cox) test). **e–g**, Expression of IL-10 (**e**), TNF-α (**f**) and CXCL1/KC (**g**) in the brain of the G422-bearing mice before and after surgical treatment for 10 d ($n = 2$ independent experiments). **h–j**, Expression of IL-10 (**h**), TNF-α (**i**) and CXCL1/KC (**j**) in the serum of the G422-bearing mice before and after surgical treatment for 3 d ($n = 2$ independent experiments). In **e–j**, the data are shown as mean ± s.d.

applied the fluorescent glioma model generated by the stable green fluorescent protein (GFP)-transfected G422 (GFP-G422) cells to assess the efficiency of surgical tumour resection. At 16 days post-implantation of GFP-G422 cells, the GFP signals in the brains before and after surgery were detected (Supplementary Fig. 19a). The tumour resection efficiency was determined to be about 96% by a quantitative region-of-interest (ROI) analysis on the GFP signal variation after surgery. The remaining infiltrating GFP-G422 cells were observed in the normal brain parenchyma after surgery (Supplementary Fig. 19b).

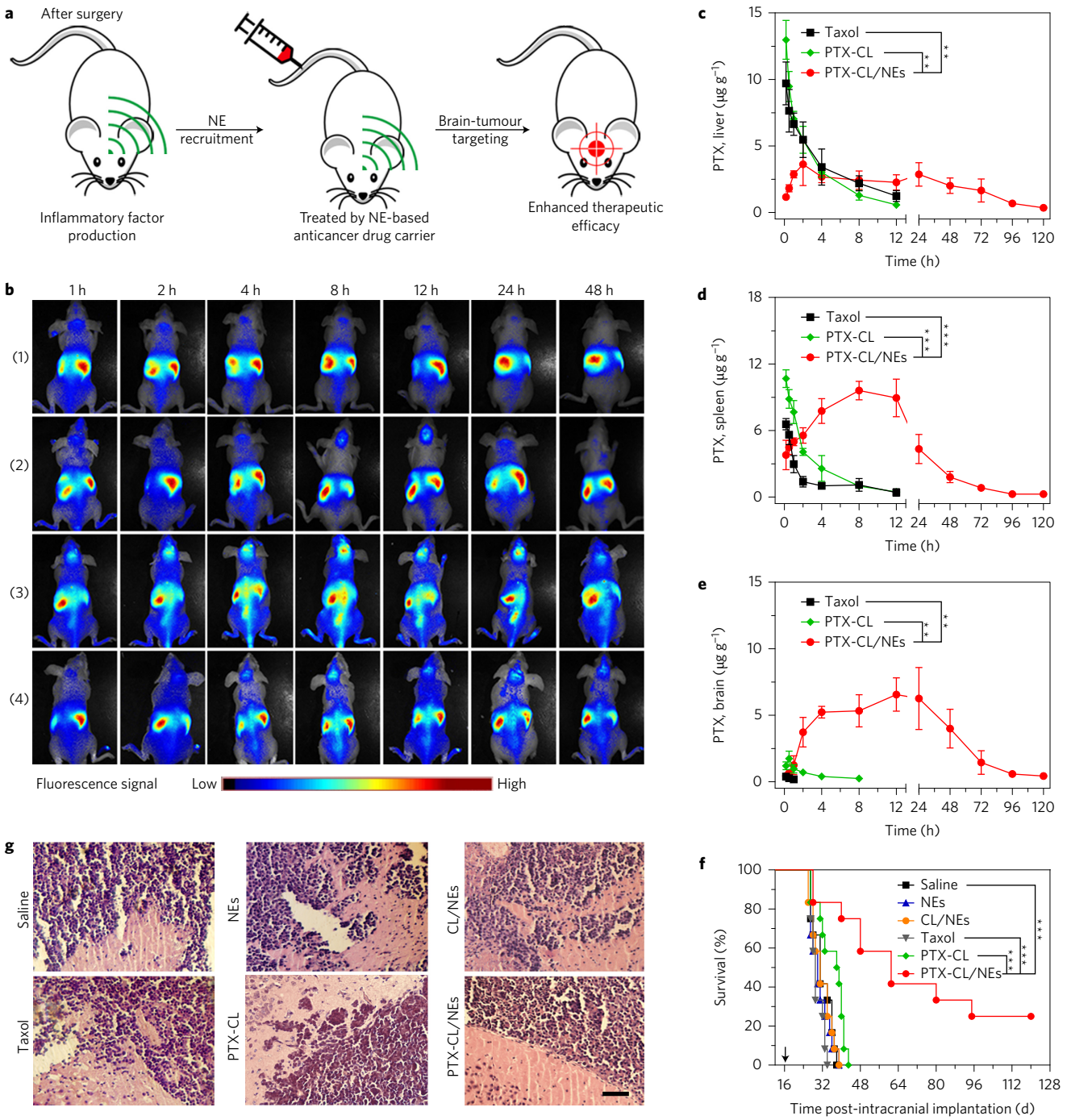

Figure 5 | PTX-CL/NEs are recruited to the brain and mediate an antitumour effect. a, Schematic illustration of NE-mediated anticancer drug delivery for inhibiting glioma recurrence after surgical tumour removal. **b**, *In vivo* fluorescence imaging of the normal mice (1), G422-bearing mice (2), surgically treated G422-bearing mice (3) and the sham-operated mice (4) after intravenous administration of PTX-CL/DiR-NEs at a dosage of 5×10^6 cells/mouse over time. **c**–**e**, Quantification of the PTX distribution in the liver (**c**), spleen (**d**) and brain (**e**) of the surgically treated G422-bearing mice after intravenous administration of different PTX formulations at a PTX dosage of 5 mg kg^{-1} over time. Data are shown as mean ± s.d. ($n = 3$ independent experiments). $^{**}P < 0.01$, $^{***}P < 0.001$ (two-tailed Student's *t*-test). **f**, Survival curves of the surgically treated G422-bearing mice after intravenous administration of saline, the blank NEs (5×10^6 cells/mouse), CL/NEs without PTX (5×10^6 cells/mouse), Taxol (10 mg kg^{-1} PTX), PTX-CL (10 mg kg^{-1} PTX) and PTX-CL/NEs (5×10^6 cells/mouse, equivalent to 5 mg kg^{-1} PTX) ($n = 12$ mice per group). Arrow indicates the time of the surgery. $^{***}P < 0.001$ (log-rank (Mantel–Cox) test). **g**, Histological observation of the brain collected from the surgically treated G422-bearing mice after treatment with different formulations. Scale bar, 100 μm.

The postoperative G422 glioma recurrence was monitored using histological analysis (Supplementary Fig. 20). At two days post-surgery, several small islands of tumour cells clearly remained in the normal brain parenchyma around the surgical cavity. After 12 days, an apparent recurrence was found in the surgical cavity in the mice. The surgical treatment significantly increased the survival rate of the mice (Fig. 4d). Unfortunately, all the surgically treated G422-bearing mice died within 22 days through malignant glioma recurrence.

The expression levels of inflammatory cytokines were quantified in the brain and serum of the G422-bearing mice after surgery. The level of IL-10 as an anti-inflammatory cytokine in the surgically treated G422-bearing mice increased, but was lower than that of

the sham-operated mice (Fig. 4e). In contrast, both TNF-α and CXCL1/KC, as pro-inflammatory cytokines, manifested a significantly elevated expression (Fig. 4f,g), which could be observed in the inflamed brain of the surgically treated G422-bearing mice (Supplementary Fig. 21). The lower IL-10 level, as well as the higher TNF-α and CXCL1/KC levels, were correlatively determined in the blood on the inflammatory response (Fig. 4h–j). These cytokines showed a similar tendency of change in the brain and serum of another two glioma models with the rat glioblastoma (C6) and human glioblastoma (U-87 MG (ref. 47)) tumours after surgery (Supplementary Figs 22 and 23), which confirms that the surgery-induced upregulation of cytokines was not model dependent. These results indicate that an inflammatory stress reaction occurs after the surgical tumour removal, and increased amounts of the relevant cytokines are retained in the brain for a long period, which can facilitate attracting the circulating PTX-CL/NEs after systemic administration to the site of the inflamed brain.

Brain-tumour targeting and antitumour effect

The brain-tumour targetability and therapeutic efficacy of PTX-CL/NEs were evaluated on two mouse glioma surgical resection models (Fig. 5a) implanted with G422 and C6 cells (Supplementary Fig. 24). We first monitored the *in vivo* biodistribution of DiR-labelled PTX-CL/NEs (PTX-CL/DiR-NEs) after intravenous administration in different mouse models. PTX-CL/DiR-NEs presented a significantly stronger capability of brain targeting in the surgically treated glioma-bearing mice than either the untreated glioma-bearing or the sham-operated mice (Fig. 5b and Supplementary Figs 25 and 26), as further confirmed by a quantitative ROI analysis (Supplementary Fig. 27). The highest signal of DiR from the PTX-CL/DiR-NEs was determined in the tumour region of the brain collected from the surgically treated glioma-bearing mice (Supplementary Fig. 28). Furthermore, we investigated whether NEs could target the remaining invading glioma cells distal to the surgical cavity. At 12 hours after injection of PTX-CL/DiR-NEs into the surgically treated GFP-G422-bearing mice, a strong signal of DiR was clearly observed not only around the surgical cavity, but also partly co-localized with the signal of the infiltrating GFP-G422 cells inside the normal brain parenchyma (Supplementary Fig. 29). As the time extended to 24 hours, more PTX-CL/DiR-NEs migrated to the GFP-G422 cells, which was maintained up to 96 hours. These data suggest that the tumour-associated inflammatory response that was amplified after surgery resulted in an enhanced brain-tumour-targeting effect of the NEs, which were able to target the infiltrating glioma cells.

The amount of PTX delivered by the PTX-CL/NEs in different organs of the surgically treated G422-bearing mice was quantified. PTX-CL/NEs presented a delayed accumulation in the liver compared with Taxol and PTX-CL (Fig. 5c). A relatively higher PTX accumulation was determined in the spleen (Fig. 5d) rather than in other organs (Supplementary Fig. 30), mainly because of the intrinsic migratory capacity of NEs to this reservoir[48]. More significantly, PTX-CL/NEs rendered an extremely high PTX accumulation in the inflamed brain (Fig. 5e). PTX was hardly delivered into the brain by Taxol, and PTX-CL also showed limited PTX accumulation, although CLs can target the angiogenic endothelial cells in the tumour and inflammation[49]. The area under the concentration versus time curve (AUC) in the brain (AUC_{brain}) for the PTX of PTX-CL/NEs was 1,162- and 86-fold higher than that of Taxol and PTX-CL, respectively (Supplementary Table 1). The brain-targeting efficiencies of PTX-CL/NEs were determined as all greater than one (Supplementary Fig. 31), which confirms the superior brain-tumour targetability of PTX-CL/NEs mediated by the postoperative inflammatory response. We further determined the quantity of DiR in the organs to indicate distribution profiles of NEs in different models (Supplementary Fig. 32). PTX-CL/DiR-NEs showed the highest AUC_{brain} of the DiR signal and the brain-targeting efficiency in the brain of the surgically treated G422-bearing mice than three other models, which verified that the higher accumulation of PTX in the brain of the surgically treated glioma-bearing mice resulted from the higher presence of NEs after intravenous administration of PTX-CL/NEs.

The longest survival was observed for the G422-bearing mice treated with tumour resection followed by treatment with PTX-CL/NEs at a PTX dosage half that of Taxol and PTX-CL (Fig. 5f). The 50% survival rate was up to 61 days compared with 29 days for Taxol and 38 days for PTX-CL. Treatment with the blank NEs and CL/NEs showed no amelioration of survival. No noticeable reduction in the body weight of the mice was found during treatment with PTX-CL/NEs (Supplementary Fig. 33). No neurological morbidity or other side effects were observed in the mice receiving PTX-CL/NE treatment after surgery. Treatment with PTX-CL/NEs did not result in any significant change in the liver-enzyme levels in the serum compared with the treatment with saline (Supplementary Fig. 34). We also utilized a histological analysis to examine the shape and margin of the recurrent tumours in the brain at the onset of neurological deficits (Fig. 5g). The tumour collected from the mice treated with PTX-CL/NEs exhibited a round shape and well-delineated margin with no signs of local infiltration into the normal brain parenchyma. In contrast, an irregular shape and margin with many invading tumour cells and islands of tumour cells were notably visible in all the brains of the mice treated with other formulations. During four months of monitoring, 25% of the studied mice survived after treatment with PTX-CL/NEs. However, these mice were not fully cured. Several small islands of tumour cells were detected in the brains of the surviving mice (Supplementary Fig. 35), which indicates that the systemic administration of PTX-CL/NEs after surgical tumour resection may not completely cure the mice, but can significantly improve mice survival and delay glioma recurrence. Although an increase in the luminescence signal of Luc-G422 cells after tumour removal was hardly observable (Supplementary Fig. 18b), treatment with PTX-CL/NEs also showed the greatest inhibitory effect on tumour relapse with the longest survival period (Supplementary Fig. 18c). Similarly, several tumour cells present in the brain of surviving mice were examined (Supplementary Fig. 18d). Also, no pathological variation was observed in the main organs after treatment with PTX-CL/NEs (Supplementary Fig. 36). Moreover, treatment with PTX-CL/NEs did not significantly prolong the survival of the non-surgically treated G422-bearing mice no matter whether the mice were pre-injected intratumourally with human IL-8, which is able to recruit the mouse NEs[50] (Supplementary Fig. 37). In addition, PTX-CL/NEs exhibited a superior capacity to extend the survival and slow the glioma recurrence on the surgically treated C6-bearing mice (Supplementary Figs 38 and 39).

Conclusions

We have developed a cell-based anticancer DDS using the physiological characteristics of native NEs to enhance the therapeutic potential for postoperative glioma treatment. Unlike traditional nanoparticles that target accumulation at the tumour site based on passive targeting, known as the enhanced permeability and retention effect[51], or active targeting via ligand–receptor interactions[52], the NE-mediated DDS possesses the capacity to recognize the post-operative inflammatory signals, such as IL-8 and CXCL1/KC (refs 53,54), and deliver the chemotherapeutics to the infiltrating glioma cells in a spontaneous and on-demand manner. NEs that carry liposomal PTX, PTX-CL/NEs, not only home in on the surgical cavity, but also are capable of targeting the infiltrating glioma cells distal to the surgical region. The excessive activation of NEs by the upregulated inflammatory cytokines in the inflamed brain results in disruption of the NEs and release of NETs, fibrous

extracellular matrices composed primarily of DNA from the NEs[32], which renders a concomitant release of liposomes to deliver PTX into the remaining invading tumour cells. Treatment with PTX-CL/NEs presents superior inhibitory effects on tumour recurrence in surgically treated glioma mouse models, but no significant enhancement on suppressing the tumour growth of mice with primary gliomas, which indicates that amplification of the inflammatory signals after surgery facilitates enhancing the brain-tumour targeting and therapeutic efficacy of PTX-CL/NEs. Such treatment efficiently slowed the recurrent growth with a significantly improved survival rate but an incomplete inhibition. The surviving mice were not fully cured during the studied monitoring period, and several islands of tumour cells were still detected in the normal brain parenchyma. Possible reasons for the incomplete cure by the PTX-CL/NE treatment include PTX resistance of the recurrent glioma cells, or the presence of escaping tumour cells, which shows that a potential application of combination treatment may be considered to achieve an ideal efficacy. We believe this strategy will offer new opportunities to explore endogenous immunocytes as delivery vehicles, which may have a potential to be translated into clinically utilizing NEs harvested from humans in the future.

Methods

Methods and any associated references are available in the online version of the paper.

Received 25 November 2014; accepted 5 March 2017; published online 19 June 2017

References

1. Gladson, C. L., Prayson, R. A. & Liu, W. M. The pathobiology of glioma tumors. *Annu. Rev. Pathol.* **5,** 33–50 (2010).
2. Agrawal, N. S. *et al.* Current studies of immunotherapy on glioblastoma. *J. Neurol. Neurosurg.* **1,** 1000104 (2014).
3. Huse, J. T. & Holland, E. C. Targeting brain cancer: advances in the molecular pathology of malignant glioma and medulloblastoma. *Nat. Rev. Cancer* **10,** 319–331 (2010).
4. Park, J. K. *et al.* Scale to predict survival after surgery for recurrent glioblastoma multiforme. *J. Clin. Oncol.* **28,** 3838–3843 (2010).
5. Lacroix, M. *et al.* A multivariate analysis of 416 patients with glioblastoma multiforme: prognosis, extent of resection, and survival. *J. Neurosurg.* **95,** 190–198 (2001).
6. Ballabh, P., Braun, A. & Nedergaard, M. The blood–brain barrier: an overview: structure, regulation, and clinical implications. *Neurobiol. Dis.* **16,** 1–13 (2004).
7. Stern, J. I. & Raizer, J. J. Chemotherapy in the treatment of malignant gliomas. *Expert Rev. Anticancer Ther.* **6,** 755–767 (2006).
8. Peer, D. *et al.* Nanocarriers as an emerging platform for cancer therapy. *Nat. Nanotech.* **2,** 751–760 (2007).
9. Mo, R. & Gu, Z. Tumor microenvironment and intracellular signal-activated nanomaterials for anticancer drug delivery. *Mater. Today* **19,** 274–283 (2016).
10. Lu, Y., Aimetti, A. A., Langer, R. & Gu, Z. Bioresponsive materials. *Nat. Mater. Rev.* **1,** 16075 (2016).
11. Mangraviti, A., Gullotti, D., Tyler, B. & Brem, H. Nanobiotechnology-based delivery strategies: new frontiers in brain tumor targeted therapies. *J. Control. Release* **240,** 443–453 (2016).
12. Jain, R. K. & Stylianopoulos, T. Delivering nanomedicine to solid tumors. *Nat. Rev. Clin. Oncol.* **7,** 653–664 (2010).
13. Huynh, G. H., Deen, D. F. & Szoka, F. C. Barriers to carrier mediated drug and gene delivery to brain tumors. *J. Control. Release* **110,** 236–259 (2006).
14. Pierige, F., Serafini, S., Rossi, L. & Magnani, M. Cell-based drug delivery. *Adv. Drug Deliv. Rev.* **60,** 286–295 (2008).
15. Batrakova, E. V., Gendelman, H. E. & Kabanov, A. V. Cell-mediated drug delivery. *Expert Opin. Drug Deliv.* **8,** 415–433 (2011).
16. Gu, L. & Mooney, D. J. Biomaterials and emerging anticancer therapeutics: engineering the microenvironment. *Nat. Rev. Cancer.* **16,** 56–66 (2016).
17. Bernardes-Silva, M., Anthony, D. C., Issekutz, A. C. & Perry, V. H. Recruitment of neutrophils across the blood–brain barrier: the role of E- and P-selectins. *J. Cereb. Blood Flow Metab.* **21,** 1115–1124 (2001).
18. Joice, S. L. *et al.* Modulation of blood–brain barrier permeability by neutrophils: *in vitro* and *in vivo* studies. *Brain Res.* **1298,** 13–23 (2009).
19. Fossati, G. *et al.* Neutrophil infiltration into human gliomas. *Acta Neuropathol.* **98,** 349–354 (1999).
20. Qin, J. *et al.* Surface modification of RGD-liposomes for selective drug delivery to monocytes/neutrophils in brain. *Chem. Pharm. Bull.* **55,** 1192–1197 (2007).
21. Mishalian, I. *et al.* Tumor-associated neutrophils (TAN) develop pro-tumorigenic properties during tumor progression. *Cancer Immunol. Immunother.* **62,** 1745–1756 (2013).
22. Gregory, A. D. & Houghton, A. M. Tumor-associated neutrophils: new targets for cancer therapy. *Cancer Res.* **71,** 2411–2416 (2011).
23. Salmaggi, A. *et al.* Intracavitary vEGF, bFGF, IL-8, IL-12 levels in primary and recurrent malignant glioma. *J. Neurooncol.* **62,** 297–303 (2003).
24. Brat, D. J., Bellail, A. C. & Van Meir, E. G. The role of interleukin-8 and its receptors in gliomagenesis and tumoral angiogenesis. *Neuro. Oncol.* **7,** 122–133 (2005).
25. Ryuto, M. *et al.* Induction of vascular endothelial growth factor by tumor necrosis factor α in human glioma cells. Possible roles of SP-1. *J. Biol. Chem.* **271,** 28220–28228 (1996).
26. Nabors, L. B. *et al.* Tumor necrosis factor α induces angiogenic factor up-regulation in malignant glioma cells: a role for RNA stabilization and HuR. *Cancer Res.* **63,** 4181–4187 (2003).
27. Kolaczkowska, E. & Kubes, P. Neutrophil recruitment and function in health and inflammation. *Nat. Rev. Immunol.* **13,** 159–175 (2013).
28. Postma, T. J. *et al.* A phase II study of paclitaxel in chemonaïve patients with recurrent high-grade glioma. *Ann. Oncol.* **11,** 409–413 (2000).
29. Lidar, Z. *et al.* Convection-enhanced delivery of paclitaxel for the treatment of recurrent malignant glioma: a phase I/II clinical study. *J. Neurosurg.* **100,** 472–479 (2004).
30. Ley, K., Laudanna, C., Cybulsky, M. I. & Nourshargh, S. Getting to the site of inflammation: the leukocyte adhesion cascade updated. *Nat. Rev. Immunol.* **7,** 678–689 (2007).
31. Brinkmann, V. *et al.* Neutrophil extracellular traps kill bacteria. *Science* **303,** 1532–1535 (2004).
32. Keshari, R. S. *et al.* Cytokines induced neutrophil extracellular traps formation: implication for the inflammatory disease condition. *PLoS ONE* **7,** e48111 (2012).
33. Boxio, R., Bossenmeyer-Pourié, C., Steinckwich, N., Dournon, C. & Nüsse, O. Mouse bone marrow contains large numbers of functionally competent neutrophils. *J. Leukoc. Biol.* **75,** 604–611 (2004).
34. Anderson, D. C., Miller, L. J., Schmalstieg, F. C., Rothlein, R. & Springer, T. A. Contributions of the Mac-I glycoprotein family to adherence-dependent granulocyte functions: structure–function assessments employing subunit-specific monoclonal antibodies. *J. Immunol.* **137,** 15–27 (1986).
35. Diamond, M. S. & Springer, T. A. A subpopulation of Mac-1 (CD11b/CD18) molecules mediates neutrophil adhesion to ICAM-1 and fibrinogen. *J. Cell Biol.* **120,** 545–556 (1993).
36. Marasco, W. *et al.* Purification and identification of formyl-methionyl-leucyl-phenylalanine as the major peptide neutrophil chemotactic factor produced by *Escherichia coli*. *J. Biol. Chem.* **259,** 5430–5439 (1984).
37. Heit, B., Liu, L., Colarusso, P., Puri, K. D. & Kubes, P. Pi3k accelerates, but is not required for, neutrophil chemotaxis to fMLP. *J. Cell Sci.* **121,** 205–214 (2008).
38. Paulsson, J. M., Jacobson, S. H. & Lundahl, J. Neutrophil activation during transmigration *in vivo* and *in vitro*: a translational study using the skin chamber model. *J. Immunol. Methods* **361,** 82–88 (2010).
39. Akahoshi, T. *et al.* Rapid induction of neutrophil apoptosis by sulfasalazine: implications of reactive oxygen species in the apoptotic process. *J. Leukoc. Biol.* **62,** 817–826 (1997).
40. Fuchs, T. A. *et al.* Novel cell death program leads to neutrophil extracellular traps. *J. Cell Biol.* **176,** 231–241 (2007).
41. Li, G. *et al.* Permeability of endothelial and astrocyte cocultures: *in vitro* blood–brain barrier models for drug delivery studies. *Ann. Biomed. Eng.* **38,** 2499–2511 (2010).
42. Brown, R. C., Morris, A. P. & O'Neil, R. G. Tight junction protein expression and barrier properties of immortalized mouse brain microvessel endothelial cells. *Brain Res.* **1130,** 17–30 (2007).
43. Ju, C. *et al.* Sequential intra-intercellular nanoparticle delivery system for deep tumor penetration. *Angew. Chem. Int. Ed.* **53,** 6253–6258 (2014).
44. Hol, J., Wilhelmsen, L. & Haraldsen, G. The murine IL-8 homologues KC, MIP-2, and LIX are found in endothelial cytoplasmic granules but not in Weibel–Palade bodies. *J. Leukoc. Biol.* **87,** 501–508 (2010).
45. Chauffier, K. *et al.* Induction of the chemokine IL-8/Kc by the articular cartilage: possible influence on osteoarthritis. *Joint Bone Spine* **79,** 604–609 (2012).
46. Bello, L. *et al.* Suppression of malignant glioma recurrence in a newly developed animal model by endogenous inhibitors. *Clin. Cancer Res.* **8,** 3539–3548 (2002).
47. Allen, M., Bjerke, M., Edlund, H., Nelander, S. & Westermark, B. Origin of the U87MG glioma cell line: good news and bad news. *Sci. Transl. Med.* **8,** 354re3 (2016).
48. Summers, C. *et al.* Neutrophil kinetics in health and disease. *Trends Immunol.* **31,** 318–324 (2010).
49. Thurston, G. *et al.* Cationic liposomes target angiogenic endothelial cells in tumors and chronic inflammation in mice. *J. Clin. Invest.* **101,** 1401–1413 (1998).

50. Partida-Sánchez, S. *et al.* Cyclic ADP-ribose production by CD38 regulates intracellular calcium release, extracellular calcium influx and chemotaxis in neutrophils and is required for bacterial clearance *in vivo*. *Nat. Med.* **7,** 1209–1216 (2001).
51. Iyer, A. K., Khaled, G., Fang, J. & Maeda, H. Exploiting the enhanced permeability and retention effect for tumor targeting. *Drug Discov. Today* **11,** 812–818 (2006).
52. Bertrand, N., Wu, J., Xu, X., Kamaly, N. & Farokhzad, O. C. Cancer nanotechnology: the impact of passive and active targeting in the era of modern cancer biology. *Adv. Drug Deliv. Rev.* **66,** 2–25 (2014).
53. De Filippo, K. *et al.* Mast cell and macrophage chemokines CXCL1/CXCL2 control the early stage of neutrophil recruitment during tissue inflammation. *Blood* **121,** 4930–4937 (2013).
54. Mantovani, A., Cassatella, M. A., Costantini, C. & Jaillon, S. Neutrophils in the activation and regulation of innate and adaptive immunity. *Nat. Rev. Immunol.* **11,** 519–531 (2011).

Acknowledgements

This work was supported by the National Natural Science Foundation of China (81273468, 81473153), the National Basic Research Program of China (2015CB755500), the State Key Laboratory of Natural Medicines at China Pharmaceutical University (SKLNMZZCX201401) and the 111 Project from the Ministry of Education of China and the State Administration of Foreign Expert Affairs of China (No. 111-2-07). We thank P. Shen, Y. Yang, X. Liu and L. Liu for valuable comments and suggestions.

Author contributions

J.X. designed and performed the experiments, and analysed the data. Z.Z., L.Z., S.S., Y.W. and Z.W. performed the experiments. L.X. and L.K. characterized the cationic lipid. L.W. synthesized the cationic lipid. H.S. and Q.P. analysed the data of the evaluation of the physiological functions of NEs. R.M. designed the experiments, analysed and interpreted the data, and wrote the manuscript. C.Z. conceived and supervised the project, and analysed and interpreted the data. All the authors discussed the results and reviewed the manuscript.

Additional information

Supplementary information is available in the online version of the paper. Reprints and permissions information is available online at www.nature.com/reprints. Publisher's note: Springer Nature remains neutral with regard to jurisdictional claims in published maps and institutional affiliations. Correspondence and requests for materials should be addressed to R.M. and C.Z.

Competing financial interests

The authors declare no competing financial interests.

Methods

Isolation of mature murine NEs from bone marrow. Mature NEs were isolated from murine bone marrow using a modified method. Briefly, the bones were immersed in RPMI 1640 medium after removal of the muscle and sinew. Bone marrow was flushed from the bone with phosphate-buffered saline (PBS), centrifuged at 200*g* for 3 min and resuspended in PBS. The unicellular suspension was added into a Percoll mixture solution consisting of 55, 65 and 78% (v:v) Percoll in PBS, followed by centrifugation at 500*g* for 30 min. The mature NEs were recovered at the interface of the 65 and 78% fractions and washed by ice-cold PBS thrice. The yield was quantified using a haemacytometer (Bright-Line, Sigma-Aldrich). The viability of the obtained mature NEs was calculated by trypan blue exclusion, and the purity was determined using immunofluorescence double staining with fluorescein isothiocyanate (FITC)-conjugated Ly-6G/Ly-6C (Gr-1) antibody (250 ng ml^{-1}) (BioLegend) and phycoerythrin (PE)-conjugated MAIR-IV (CLM-5) antibody (1 μg ml^{-1}) (BioLegend). The morphology of NEs stained with Wright-Giemsa (Jiancheng Bio) was observed by an optical microscope (Ts2R, Nikon).

Preparation of PTX-CL/NEs. PTX-CL/NEs were obtained by incubating NEs with PTX-CL. Briefly, the mature NEs (1×10^5 cells ml^{-1}) were seeded in a sterile tube. After culture with the FBS free medium for 1 h, NEs were incubated with PTX-CL at a PTX concentration of 50 μg ml^{-1} at 37 °C for 50 min. After washing with ice-cold PBS thrice, the PTX-CL/NE suspension was obtained and used immediately for the subsequent study. The concentration of PTX in PTX-CL/NEs was determined using HPLC. To quantify the amount of PTX in the PTX-CL/NEs, PTX-CL/NEs were disrupted by a cell lysis buffer (Beyotime) to release PTX from the NEs. The cell lysate was collected and centrifuged at 10,000*g* for 5 min. The supernatant (50 μl) was mixed with 200 μl of methanol, vortexed for 5 min and centrifuged at 10,000*g* for 10 min. The supernatant (20 μl) was injected into the HPLC system for quantification. For the preparation of NEs loaded with Cou6-CL (Cou6-CL/NEs), NEs (1×10^5 cells ml^{-1}) were incubated with Cou6-CL at a Cou6 concentration of 40 ng ml^{-1} at 37 °C for 30 min. The subsequent procedure was similar to that for PTX-CL/NEs.

Evaluation of physiological functions of PTX-CL/NEs. The physiological activities of PTX-CL/NEs were evaluated, including the inflammation-responsive expression of the specific protein CD11b, chemotaxis and superoxide-anion production. The blank NEs or PTX-CL/NEs were incubated with different concentrations of fMLP at 37 °C for 0.5 h. After washing with ice-cold PBS thrice, the NE formulations were incubated with the PE-conjugated CD11b antibody (20 ng ml^{-1}) (BioLegend) for 30 min and then washed with ice-cold PBS thrice. The fluorescence intensity was determined using flow cytometry (BD FACSCanto, BD Biosciences).

The chemotaxis of PTX-CL/NEs was investigated using a transwell migration assay (transwell polycarbonate membrane: 3 μm pore size, 6.5 mm diameter and 0.33 cm^2 membrane surface area) (Corning). Briefly, different NE formulations (the blank NEs, Taxol/NEs, CL/NEs and PTX-CL/NEs) (2×10^5 cells) were added to the upper chamber of the transwell. The lower chamber of the transwell was filled with a fetal bovine serum (FBS) free culture medium containing different concentrations of fMLP. After 0.5 h of incubation, the cells in the lower chamber were harvested and the numbers were counted using a haemacytometer. The chemotaxis index ($(N_{fMLP} - N_{control})/N_{control}$)) was calculated, where N_{fMLP} and $N_{control}$ are the counted numbers of NEs in the lower chamber after incubating with each NE formulation in the presence of fMLP and the blank NEs in the absence of fMLP, respectively.

The inflammation-mediated superoxide-generating capability of PTX-CL/NEs was examined using dihydroethidium (Beyotime). Different NE formulations (the blank NEs, Taxol/NEs, CL/NEs and PTX-CL/NEs) (1×10^5 cells) were incubated with fMLP (1 μM) at 37 °C for 0.5 h, followed by washing with ice-cold PBS twice and then stained with dihydroethidium at 37 °C for 0.5 h. After washing with ice-cold PBS twice, the fluorescence intensity was measured using flow cytometry.

Release of PTX from PTX-CL/NEs at the site of inflammation. The *in vitro* release properties of PTX from PTX-CL/NEs were evaluated under different conditions, including the normal physiological condition, during the process of chemotaxis responding to local inflammation, at the site of inflammation and on apoptosis. fMLP and PMA were applied to simulate the chemotactic cytokines in the blood circulation and at the site of inflammation, respectively, and sulfasalazine was used to induce the apoptosis of the NEs. Briefly, PTX-CL/NEs (1×10^6 cells/well) were seeded in 24-well plates, and then incubated with the FBS free medium that contained fMLP (10 nM), PMA (100 nM) or sulfasalazine (300 μM) for different periods (0, 2, 4, 6 and 8 h). The amounts of PTX in the NEs and released in the supernatant medium were determined using HPLC.

To further demonstrate the drug release from NEs on the PMA-induced formation of NET, Cou6-CL/NEs were treated with fMLP or PMA and observed using confocal laser scanning microscopy (CLSM) (TCS SP5, Leica). Cou6-CL/NEs (1×10^6 cells/well) were seeded in confocal dishes (NEST), and then incubated with the FBS free medium containing fMLP (10 nM) or PMA (100 nM) for 0 and 8 h. Subsequently, the cells were stained with PI (5 μg ml^{-1}) for 30 min. After washing with ice-cold PBS twice, the cells were visualized using a fluorescence microscope (TH4-200, Olympus).

To confirm that the released PTX was encapsulated mainly in the PTX-CL, PMA-treated PTX-CL/NEs were centrifuged at 10,000*g* for 10 min, and the supernatant was added into a centrifugal filter device (100 K MWCO, Millipore), followed by centrifugation at 14,000*g* for 15 min. The amount of free PTX in the filtrate was determined using HPLC. The ratio of the encapsulated PTX to the total released PTX ($(Q_s - Q_f)/Q_s \times 100\%$) was calculated, where Q_s and Q_f are the amounts of PTX in the supernatant before centrifugation and in the filtrate after centrifugation, respectively. For transmission electron microscope (TEM) observation, the supernatant was dropped onto a copper grid (300 mesh) and stained by phosphotungstic acid (0.1% v:v). After air drying, the sample was observed by TEM (H-7650, Hitachi) at an accelerating voltage of 80 kV.

Cell culture. bEnd.3, C6 and U-87 MG cells were purchased from the American Type Culture Collection. G422, GFP-G422 and Luc-G422 cells were provided by Tongpai Biotech. All the cells were used without further authentication, but were routinely tested for mycoplasma contamination. bEnd.3, G422, GFP-G422 and Luc-G422 cells were cultured in RPMI 1640 medium. U-87 MG cells were cultured in EMEM medium. C6 cells were cultured in DMEM (low glucose) medium. All the media were supplemented with FBS (10% v:v), penicillin (100 U ml^{-1}) and streptomycin (100 μg ml^{-1}). For both the GFP-G422 and the Luc-G422 cell cultures, puromycin (4 μg ml^{-1}) was added in the media.

Chemotactic migration across the BBB. The *in vitro* BBB model was constructed with bEnd.3 cells using a transwell cell culture system. Briefly, bEnd.3 cells (1×10^5 cells/well) were seeded onto the upper chamber of the transwell pre-coated with gelatine (2% w:v) in 24-well plates, and cultured with the medium containing FBS (10% v:v). The integrity of the cell monolayer was evaluated by measuring the TEER values using a Millicell-ERS voltohmmeter (Millipore). The cell monolayers with TEER values higher than 300 Ω cm^2 were used as the BBB model for the transmigration studies.

Different PTX formulations (200 μl), such as Taxol (18 μg ml^{-1} PTX), PTX-CL (18 μg ml^{-1} PTX) and PTX-CL/NEs (2×10^5 cells, equivalent to 18 μg ml^{-1} PTX), were added to the upper chamber, and the FBS free medium with or without fMLP (10 nM) was added to the lower chamber. After 3 h of incubation, the supernatant in the upper chamber and the medium in the lower chamber were sampled, and the bEnd.3 cell layers on the membrane of the transwells were harvested. The amounts of PTX in the supernatant, intracellular and filtered compartments were determined using HPLC. The PTX ratio in each compartment was calculated compared with the feeding amount of PTX. The number of NEs in the lower chamber was also counted.

Animals and glioma surgical resection model. All the animals were treated in accordance with the Guide for Care and Use of Laboratory Animals, approved by the Animal Experimentation Ethics Committee of China Pharmaceutical University. The Institute of Cancer Research mice (male, six-weeks old) and nude mice (BALB/c, male, six-weeks old) were provided by the Comparative Medicine Center of Yangzhou University. To establish an *in situ* glioma tumour model, the mice were intracranially implanted with G422 or C6 cells (1×10^5 cells/mouse), and the nude mice were implanted with U-87 MG cells (1×10^5 cells/mouse) using an open-window technique. The tumour-bearing mice were sacrificed at different days after tumour implantation to monitor the pattern of tumour growth. The brains were harvested, fixed in paraformaldehyde in PBS (4% v:v) and stained with haematoxylin and eosin (H&E). The H&E-stained brain section was observed using an optical microscope to examine the shape of the tumour and the area of the local infiltration at the tumour periphery. The body weights and survival periods of the mice were also monitored after tumour implantation.

At 16 d (G422) or 7 d (C6) after tumour implantation, well-established tumours had formed and the tumour-bearing mice were submitted for surgical resection of the tumour. Under ×10 magnification, the tumour mass was picked up and macroscopically completely removed by a tissue microforcep using a microsurgical technique. Surgical tumour removal was undertaken until the white walls that indicated normal brain were macroscopically apparent in the surgical cavity. Haemostasis was accomplished using gelfoam, and surgical and prolonged irrigation, but coagulant was not used. The operation time was about 20 min. The mortality was lower than 5% and occurred within the first 2 d of surgery. Histological examination of the brain sections from the tumour-bearing mice 2 d (G422) or 3 d (C6) after surgery displayed that many islands of tumour cells persisted close to the surgical cavity. Small tumour masses that indicated a glioma recurrence were observed within 12 d (G422) or 7 d (C6) after surgery. The body weights and survival periods of the tumour-bearing mice were also monitored after surgery.

To monitor tumour growth intuitively, the mice were intracranially implanted with Luc-G422 cells (1×10^5 cells/mouse), and detected at 15 min post-intraperitoneal injection of luciferin (150 mg kg^{-1}) using an *in vivo* imaging system (IVIS Lumina XR). The change in the luminescence intensity of Luc-G422 cells in the brain was determined using a quantitative ROI analysis. In addition, the fluorescent glioma model generated by GFP-G422 cells was applied to assess the efficiency of surgical tumour removal. At 16 d post-implantation of GFP-G422 cells

(1×10^5 cells/mouse), the brains of the mice were harvested before and after surgery for *ex vivo* imaging, followed by ROI analysis. The efficiency of surgical tumour removal ($(1 - F/F_0) \times 100\%$) was determined, where F and F_0 are the fluorescence intensities of the GFP signal after and before surgery, respectively. The frozen brain section was further observed using CLSM to monitor the localization and distribution of the remaining invading GFP-G422 cells in the normal brain parenchyma.

Determination of inflammatory cytokine expression after surgery. The inflammatory cytokines, such as IL-10, TNF-α and CXCL1/KC, in the brain and serum of the surgically treated tumour-bearing mice were determined using an enzyme-linked immunosorbent assay (ELISA) method. The blood samples of the tumour-bearing mice before and after surgery at different times were sampled and naturally coagulated at room temperature. The serum was obtained by centrifugation at 400*g* for 20 min. The brains were harvested and weighed after the mice were sacrificed, and then homogenized in saline to a concentration of 10% (w:v). The levels of IL-10, TNF-α and CXCL1/KC in the serum and brain homogenate were assayed using the corresponding ELISA kits. The sham-operated normal mice were taken as a control, generated as follows: the skulls of the normal mice were opened and the brain poked by a microneedle. In addition, the brain of the surgically treated G422-bearing mice was harvested at different times (6 h, 2 d and 10 d) after surgery, followed by cryotomy. TNF-α and CXCL1/KC in the frozen brain section were stained with Alexa Fluor 488-conjugated TNF-α antibody (0.5 μg ml^{-1}) (Bioss) and Alexa Fluor 647-conjugated CXCL1/KC antibody (0.5 μg ml^{-1}) (Bioss), respectively, and observed using CLSM.

Brain targetability and biodistribution. PTX-CL/DiR-NEs were obtained using the same method as described above for Cou6-CL/DiR-NEs. The brain-targeting capability of PTX-CL/DiR-NEs was first investigated using a non-invasive near-infrared optical imaging technique. At 30 min post-surgery, PTX-CL/DiR-NEs (5×10^6 cells/mouse) were intravenously injected into the normal mice, tumour-bearing mice, surgically treated tumour-bearing mice and sham-operated normal mice. At predetermined time intervals, images were taken on the Maestro *in vivo* imaging system (PerkinElmer). At 48 h post-injection, the mice were sacrificed and the brains were harvested for *ex vivo* imaging. ROI was circled around the brain, and the fluorescence intensity of the DiR signal was analysed using Living Image Software.

To investigate whether NEs are able to target the remaining invading glioma cells distal to the surgical cavity, the surgically treated GFP-G422-bearing mice were intravenously injected with PTX-CL/DiR-NEs (5×10^6 cells/mouse), and the brains were harvested at different times post-injection (12, 24, 48, 72 and 96 h), followed by cryotomy and observation using CLSM.

The *in vivo* biodistribution of PTX delivered by Taxol, PTX-CL and PTX-CL/NEs was determined by quantifying the amount of PTX in different organs. Briefly, at 30 min post-surgery, the surgically treated tumour-bearing mice were intravenously injected with Taxol (5 mg kg^{-1} PTX), PTX-CL (5 mg kg^{-1} PTX) and PTX-CL/NEs (5×10^6 cells/mouse, equivalent to 5 mg kg^{-1} PTX). The mice were sacrificed at different times post-injection. Different organs, including the liver, spleen, lung, kidney and brain, were harvested and weighed. The whole brain was selected for the determination of the quantity of PTX without excluding the surgical cavity. The weighed organs were homogenized in saline. The homogenate (0.2 ml) was mixed with acetonitrile (0.2 ml), vortexed for 5 min and centrifuged at 10,000*g* for 10 min. The amount of PTX extracted in the supernatant was quantified by HPLC. AUCs were determined using Kinetica 4.4 software (Thermo). The brain-targeting efficiency ($AUC_{brain}/AUC_{other\ organs}$) was calculated after the intravenous administration of different PTX formulations. Additionally, the DiR amount in different organs, which indicated the biodistribution of the NEs, was quantified. At 30 min post-surgery, PTX-CL/DiR-NEs (5×10^6 cells/mouse, equivalent to 5 mg kg^{-1} PTX) were intravenously injected into the normal mice, G422-bearing mice, surgically treated G422-bearing mice and sham-operated normal mice, respectively. At predetermined time intervals, different organs, including the liver, spleen, lung, kidney and brain, were harvested and weighed. The whole brain was selected for determination of the quantity of DiR without excluding the surgical cavity. The weighed organs were homogenized in saline. The homogenate (0.2 ml) was mixed with acetonitrile (0.2 ml), vortexed for 5 min and centrifuged at 10,000 g for 10 min. The amount of DiR extracted in the supernatant was determined using the microplate reader (Infinite M1000 PRO, Tecan). Brain-targeting efficiency ($AUC_{brain}/AUC_{other\ organs}$) was calculated, where AUC_{brain} and $AUC_{other\ organs}$ were the AUC of the brain and of other organs after intravenous administration of PTX-CL/DiR-NEs, respectively.

Suppression of postoperative glioma recurrence. The surgically treated glioma-bearing mice were intravenously injected with Taxol (10 mg kg^{-1} PTX), PTX-CL (10 mg kg^{-1} PTX), PTX-CL/NEs (5×10^6 cells/mouse, equivalent to 5 mg kg^{-1} PTX), the blank NEs (5×10^6 cells/mouse), CL/NEs (5×10^6 cells/mouse) and saline at 1, 2, 3, 4, 6, 8 and 10 d after surgery. The body weights and survival periods of the mice were monitored during treatment. Histological analyses of brain sections were performed when neurological impairment of the mice was observed, such as full paralysis of the hindlimbs and tail and partial paralysis of the forelimbs. The H&E-stained brain sections were visualized using an optical microscope. By comparison, the non-surgically treated glioma-bearing mice were given the above formulations using the same treatment schedule. Treatment with different formulations started at 16 and 7 d post-implantation of the G422 and C6 cells, respectively. In addition, the non-surgically-treated glioma-bearing mice that received intracranial injections of IL-8 at dosages of 16, 32 and 48 pg kg^{-1} were also treated with PTX-CL/NEs (5×10^6 cells/mouse, equivalent to 5 mg kg^{-1} PTX). Treatment with different formulations started at 16 and 7 d post-implantation of G422 and C6 cells, respectively. The body weights and survival periods of the mice were monitored during treatment.

Safety evaluation. After treatment with different formulations, the blood samples of the mice were harvested. The quantities of alanine transaminase, aspartate transaminase and alkaline phosphatase in the serum were determined using the corresponding assay kits (Sigma). Histological analyses on the normal organs, including the heart, liver, spleen, lung and kidney, using H&E staining were performed.

Statistical analysis. Results are presented as mean ± s.d. All the experiments were repeated at least twice with 2–12 replicates. Error bars represent the s.d. of the mean from independent samples studied in the represented experiments. No statistical methods were used to predetermine the sample size. Animals were randomized to treatment groups prior to the initiation of the treatment, but were not blinded for outcome assessment and data analysis. No samples or animals enrolled in the experiments were excluded during analysis. Two-tailed Student's *t*-test was applied to test the statistical significance of difference between two groups, and a log-rank (Mantel–Cox) test was used to analyse the statistical significance of difference for survival analysis. Statistical significance was set at $^*P < 0.05$, $^{**}P < 0.01$ and $^{***}P < 0.001$.

Data availability. The data that support the plots within this paper and other findings of this study are available from the corresponding author on reasonable request.